

Efficient Simulation of Fluid Flow and Transport in Heterogeneous Media Using Graphics Processing Units (GPUs)

Hassan Dashtian and Muhammad Sahimi[†]

Mork Family Department of Chemical Engineering and Materials Science, University of Southern California, Los Angeles, California 90089-1211

Networks of interconnected resistors, springs and beams, or pores are standard models of studying scalar and vector transport processes in heterogeneous materials and media, such as fluid flow in porous media, and conduction, deformations, and electric and dielectric breakdown in heterogeneous solids. The computation time and required memory are two limiting factors that hinder the scalability of the computations to very large sizes. We present a dual approach, based on the use of a combination of the central processing units (CPUs) and graphics processing units (GPUs), to simulation of flow, transport, and similar problems using the network models. A mixed-precision algorithm, together with the conjugate-gradient method is implemented on a single GPU solver. The efficiency of the method is tested with a variety of cases, including pore- and random-resistor network models in which the conductances are long-range correlated, and also contain percolation disorder. Both isotropic and anisotropic networks are considered. To put the method to a stringent test, the long-range correlations are generated by a fractional Brownian motion (FBM), which we generate by a message-passing interface method. For all the cases studied an overall speed-up factor of about one order of magnitude or better is obtained, which increases with the size of the network. Even the critical slow-down in networks near the percolation threshold does not decrease the speed-up significantly. We also obtain approximate but accurate bounds for the permeability anisotropy K_x/K_y for stratified porous media.

[†]E-mail: moe@usc.edu

I. INTRODUCTION

Fluid flow and transport in heterogeneous media is an important problem [1], in view of its relevance to a wide variety of phenomena in natural and industrial processes. A partial list of such phenomena include flow through porous media [2,3], conduction and hopping transport in composite solids [4,5], mechanical properties of disordered materials [1,5], fracture of heterogeneous solids [6-8], and many more. For over four decades the standard model of a heterogeneous medium has been a random resistor or pore network (RRN and PN, respectively) in the case of flow and scalar transport, and a network of springs or beams for studying such vector transport processes as deformation and fracture propagation. Often, disorder is introduced in the model by a percolation process [9,10] by which a fraction of the bonds of the network - pores, resistors, or springs - do not allow fluid flow, or scalar or vector transport to occur, while the rest of the bonds represent the fluid flow or transport paths. Even with such a relatively simple form of disorder a wide variety of interesting phenomena occur, a detailed understanding of which requires simulating very large networks and, thus, solving very large set of flow and transport equations.

Numerous approaches, ranging from continuum to networks models, integrate [11] the complexity of heterogeneity of porous media with fluid flow. For example, the PN models discretize the void space of a porous structure into a network consisting of pore bodies (nodes or sites) connected via pore throats (bonds) - hereafter referred to as, respectively, pores and throats - and have been widely used to investigate a wide variety of phenomena related to multiphase flow [12-16]. The applications includes drying of porous media [17-19], reactive transport [20-22], dissolution [23], unstable miscible displacements and fingering phenomenon [24], grain boundary wetting [25] and gas flow in shaly formations [26,27]. The computational limitations of the PN modeling restrict, however, its application to relatively small networks.

Thus, attention has also been focused on developing efficient methods for simulating very large PNs or RRNs and solving the associated large sets of flow or transport equations. The efforts has led to the development of the transfer-matrix method [28-30], and coarsening the disordered PNs or RRNs based on wavelet transformations and then solving a significantly-reduced number of equations [31]. With the exception of the wavelet coarsening method, which is efficient both near [33,34] and away from the percolation threshold [31,32], all the

aforementioned methods are efficient only if the PN or RRN is near the percolation threshold. Aghaei and Piri [35] developed a computational strategy for simulating multiphase flows in porous media that is capable of simulating large PNs. Their approach is, however, a massively parallel scheme.

In practice, many heterogeneous media do not contain percolation-type disorder or, if they do, their disorder is not random but highly correlated. Moreover, with the advent of sophisticated experimental techniques, such as x-ray computed tomography [36-38], it is now possible to obtain detailed data for the morphology of heterogeneous media. Taking proper account of the correlations and utilizing the detailed data in the model entails employing a high-resolution PN or RRN with several million nodes, a still daunting task. Moreover, the problem is much more difficult when one must solve unsteady-state problems over a period of time, which entails solving a very large number of equations for thousands of time steps.

In this paper we present an efficient approach to PN or RRN modeling, which is based on graphic processing units (GPUs) that have opened up a new approach for high performance computing, particularly for the researchers who do not have access to massively-parallel machines with a large number of nodes, or to vector supercomputers. The GPUs were originally designed to analyze three-dimensional graphic images. To achieve extremely high performance with geometric data, the GPUs have been designed with simple and tiny processors. More modules are used for data processing, but not for the data cache, nor for the flow control. Hence, by design the GPUs are very different from typical computations with central-processing units (CPU), and are ideal for highly intensive and parallelized calculations, if the computational algorithm can take advantage of their special features. In facilitating nongraphical calculations on its graphic units, Nvidia Corporation released Compute Unified Device Architecture (CUDA) [39]. Several groups have tested the performance of CUDA parallel computing in various calculations [40-46].

II. PORE AND RANDOM-RESISTOR NETWORKS

The first step in the PN/RRN modeling is to generate the networks. It was suggested [3,47] a long time ago that many natural porous media exhibit long-range correlations. Such correlations, which influence the percolation [48] and flow and transport properties of porous media [37,49-52], follow the statistics of fractional Browning motion (FBM) [53], a nonstation-

ary stochastic process. Thus, in addition to a random distribution of the pores' or resistors' conductances, we also use the FBM to generate correlated conductances, or throats' size, in the PN or the RRN. We use a square network in which each bond represents a throat with an effective radius r , or a resistor, selected from a statistical distribution. The bonds' length ℓ is assumed to be constant, although it poses no difficulty to select it from a statistical distribution as well. The bonds' radii (or conductances) are selected from a FBM. An efficient method for generating a FBM array is through its power spectrum $S(\boldsymbol{\omega})$, which for 2D systems is given by

$$S(\boldsymbol{\omega}) = \frac{a}{(\omega_x^2 + \omega_y^2)^{H+1}}, \quad (1)$$

where a is a constant, while ω_x and ω_y are the Fourier components in the x and y directions. Here, H is the Hurst exponent such that for $H > 0.5$ ($H < 0.5$) one has positive (negative) correlations, while $H = 0.5$ represents the case in which the successive increments of the FBM are completely random. Due to stratification, many porous media are anisotropic. To introduce the anisotropy, we follow Ansari-Rad *et al.* [54] and generalize the power spectrum to

$$S(\boldsymbol{\omega}) = \frac{b}{(\beta_x \omega_x^2 + \beta_y \omega_y^2)^{H+1}}. \quad (2)$$

Here, β_x and β_y are the anisotropy parameters, and b is a constant. To generate anisotropy induced by layering with the layers being parallel to the x direction, we set $\beta_x/\beta_y > 1$. For large PNs that we utilize in the present study, however, generating a large FBM array is computationally expensive, because as the size of the PN increases, the computation and required memory increase exponentially, if sequential programming is used for generating the FBM. Thus, to make the running time manageable, we used message-passing interface (MPI) strategy and generated the FBM algorithm as a parallel scheme in the GPU solver (see below).

The most time-consuming part of setting up a PN/RRN is generation of a 2D FBM by a fast Fourier transform (FFT) that computes the spectral density, Eq. (2), with a time complexity of $\mathcal{O}(N \log_2 N)$. Another main issue associated with the sequential implementation of the FBM algorithm is that, for large network sizes N , huge memory is required (see Table I below). To address the problem, we parallelized the program by using the message-passing interface (MPI) strategy on four processes numbered (0, 1, 2, 3); see Fig. 1. Each processor executes a part of the FBM generation algorithm, and then sends the results to the root process, number 0 in Fig. 1. In Table I we report the performance of the MPI implementation of the generation of

the 2D FBM fields, and the PN/RRN of various sizes, which indicate that the efficiency and speed-up both increase as the size increases. Let us emphasize that generation of large FBM arrays by the MPI strategy is, to our knowledge, new. Given the wide applicability of the FBM, our algorithm makes it possible to generate very long FBM array, a difficult problem.

Table 1: Efficiency and speed-up of the MPI implementation of FBM algorithm on four processes. The times are in seconds

Array Size	Required Memory (GB)	Time (Sequential)	Time (MPI)	Speed-up	Efficiency
2^{24}	0.128	1.2	0.4	2.8	0.71
2^{28}	2	8.0	2.7	2.9	0.73
2^{30}	8	71.6	20.6	3.5	0.87

We then used the generated PN/RRN as the input to the GPU-based solver. Solving for the pressure/voltage distribution consists of the CG algorithm, which is matrix operation, well suited for the GPUs. Several PNs/RRN were generated with various values of the Hurst exponent H , the anisotropy parameter β_x/β_y , and network sizes N . In Fig. 2 we present samples of the generated PNs/RRN in which the conductances vary over two orders of magnitude.

Assuming steady-state and slow (laminar) flow of an incompressible fluid, the volume flow rate in a bond ij that connects nodes i and j is given by, $q_{ij} = \pi r^4 \Delta P_{ij} / (8\mu\ell) \equiv g_{ij} \Delta P_{ij}$, where μ is the fluid's viscosity, $\Delta P_{ij} = P_j - P_i$ is the pressure drop between nodes i and j , and g_{ij} the conductance of bond ij . Writing a mass balance for every node i , one obtains, $\sum_{j \in i} q_{ij} = 0$, where the sum is over all the nodes j that are connected to node i . Thus, substituting for q_{ij} and writing the mass balance for every interior node of the network results in a set of linear equation of the following form,

$$\mathbf{GP} = \mathbf{b} , \tag{3}$$

where \mathbf{G} is the conductance matrix that depends only on the geometric properties of the network, \mathbf{P} is the nodal pressure vector (or voltage vector in the RRN) to be calculated, and \mathbf{b} is a vector related to the external boundary conditions. We impose a fixed pressure gradient on the network in one direction, and used periodic boundary conditions in the second direction.

Once the pressure (voltage) distribution in the PN is calculated, the effective permeability K (conductivity) of the network is computed based on the Darcy’s law,

$$K = \frac{Q}{S} \frac{\mu L}{\Delta P}, \quad (4)$$

where Q is the total flow rate passing through the cross section S of the PN, L is the PN’s length, and ΔP is the macroscopic pressure drop imposed on the network. A similar procedure is used to compute the effective conductivity of the RRN. The set of the equations must be solved by the conjugate-gradient (CG) method, which is the standard method in the computations with the CPU, but must be implemented in the GPU. The matrix-vector multiplication is the most dominant part in any CG iteration and, thus, it is this part that is accelerated by the GPU.

To implement the solution of the pressure/voltage distribution in a PN/RRN on GPUs, one must use CUDA programming that makes it possible to implement the CG algorithm on a single GPU. CUDA programming, as well as the memory allocation and performance from the perspective of our GPU solver kernels, is by far the most time-consuming and resource-intensive computational step in the simulations. Thus, we first describe the implementation of the algorithm on GPUs, and present its technical details.

III. CUDA and GPUs

Memory allocation in, and performance of the implementation of the algorithm are by far the most time-consuming and resource-intensive computational steps. On a GPU, parallel tasks, called threads, are scheduled and executed simultaneously in groups referred to as warps. One warp contains 32 threads that processed in parallel by one CUDA streaming multiprocessor (SM). The GPUs have many SMs that run in parallel to increase the parallelism. The threads are organized also into larger structures called blocks, which are themselves organized into grids [55]. Figure 3 shows an example of the GPU architecture hierarchy with four SM.

The CUDA memory contains various segments with different scopes and properties. All the threads have access to the same global memory. The shared memory is visible to all the threads within a block with the same lifetime as the block. Each thread has its own registers and local memory. The global memory is located in the GPU, which is the largest, but also the slowest. A programmer can allocate free global memory. In order to access the GPU memory, 32, 64, or 128 byte memory “transactions” are needed from the host to the device, which must

have the same sizes, but because they are costly in terms of their computational performance, they must be aligned and minimized. In our implementation of the CG algorithm for solving the pressure/voltage distribution in a PN or RRN, we use 1D arrays to store the elements in a vector. The local memory is allocated by the compiler for large structures that do not fit into the register space, and are part of the global memory that can be used to avoid costly memory transfers.

Despite local and global memories, shared memory is of the on-chip type and, hence, has much lower latency with higher bandwidth. The threads in a block can use shared memory to work together. For example, in the case that multiple threads in a block need to use the same data, shared memory is called upon to access the data from the global memory only once. The GPU that we use has a Kepler architecture [56], one of the most efficient high performance computing architecture in which the shared memory is 48 KB, and is organized into 32 banks. In our CUDA kernel - functions that are executed on the GPU - we store temporal variables in the shared memory. In Fig. 4 we show the concept of memory in a typical GPU.

IV. SOLVING FOR THE PRESSURE/VOLTAGE DISTRIBUTION WITH A GPU

We used the CG algorithm in both C++ and CUDA. In CUDA, the CPU is a host for GPU, with the latter called a device. Programs that are run on the CPU (host) can manage the memory on both the CPU and GPU. The CPU lunches the kernels, which and are then executed in a parallel scheme by the GPU threads. As far as the CG algorithm (as well as other iterative solvers) is concerned, the most computationally intensive kernel is the matrix-vector multiplication (MVM) kernel [57]. Most of the execution time of the main loop of a solver is spent inside the MVM kernel.

One important issue related to the GPU and CPU is the floating point accuracy of computations. In order to ensure consistent computations across platforms and to exchange floating-point data, the IEEE-754 defines basic and interchange formats to convert decimal floating point to 32 bit and 64 bit hexadecimal representations, along with their binary equivalents. The 32 and 64 bit basic binary floating point formats correspond to the C data types *float* and *double*. The GPU devices with high compute capability support both single and double precision (SP and DP, respectively) floating point computation. On CUDA the compute capability

is the “feature set,” for both the hardware and software, of the device. The higher the compute capability, the more powerful the device. The GPU device that we use in this study supports both the SP and DP.

There is, however, a significant gap between the SP and DP computations with the GPUs, as the SP calculations run much faster than the DP computations. The main bottleneck of the CG iterations is the ratio of the arithmetic operations and the data input/output steps, and the acceleration of the computations depends critically on this ratio. Thus, by using the SP data we reduced their “traffic” by a factor of two between the GPU processor and its device memory. Then, to further improve the accuracy of the CG calculations, we used a mixed-precision method, implemented by an iterative refinement algorithm. The main idea is using two types of iterative loops to obtain the true solution of the equations. First, by using the SP iteration we approach rapidly a rough solution within the inner loop. Next, iterations with the DP are used to converge to the final solution within the allowed error of the outer loop. Since the iteration loop of the CG algorithm is responsible for most of the computation time, we explain in detail the parallel implementation of this part on the GPU; see Fig. 5.

First kernel: A 1D block of size 256 is used. For each part, the size of the network is set proportional to the total number of rows and blocksize, such that there exists a thread corresponding to each row.

Second kernel: This is the sparse matrix-vector multiplication part of the computation, for which a thread is assigned to each row of matrix \mathbf{G} , which is responsible for calculating the elements of \mathbf{Z} , the vector that acts as temporary \mathbf{b} during the iteration process. Consecutive rows of \mathbf{G} have redundant access to \mathbf{P} through the calculations associated with the three main diagonals of \mathbf{G} . Thus, \mathbf{P} is cached in the shared memory for improving the access pattern. After the calculation of each entry of \mathbf{Z} in a thread, it is multiplied by its corresponding \mathbf{P} element and the result is held in the shared memory. Then, by performing a reduction operation over each block, the sums, which arise when one multiplies one row of a matrix by the column of another matrix or a vector, are calculated and stored in the global memory.

Third Kernel: For this part a thread is assigned for the calculation of each element of \mathbf{U} , \mathbf{R} , and \mathbf{Z} and, similar to the second kernel, partial result of dot products for \mathbf{R} and \mathbf{Z} are calculated and saved in the global memory for each block. Here, \mathbf{R} is the residual vector for each iteration, while \mathbf{U} represents the temporary approximate solution after each iteration.

Merging the calculations of the vectors' entries into a single kernel leads to a more efficient performance by decreasing the number of times that the global memory must be accessed. We optimized the number of threads and blocks based on the computational capability of the GPU device that we used. The number of threads per block must be a multiple of the warp size, which is 32 in all the current hardwares. We used 256 threads per block and 64 blocks in a fixed 1D grid arrangement. A loop was placed inside the threads to calculate multiple outputs per thread, so that the first iteration through all the threads is responsible for the first 2^{14} row calculations; the next iteration for the next 2^{14} row calculations, and so on.

After completion of the iteration loop, the results are saved in the shared memory. By performing a reduction operation in each block, the sum is calculated and saved in the global memory. As there are only 2^6 blocks, there will be 2^6 partial sums in the global memory, to be added together to calculate the final solution. By copying the sums' values to the main memory and performing the final sum on the CPU, a more efficient performance is achieved. Thus, a multiprocessing algorithm was designed in an attempt to use the global memory throughput more efficiently. Since most of the summation operations are performed in registers or the shared memory, there is little effect on the global memory bandwidth, and the efficacy of the mixed-precision design is not affected.

Task latency - the elapsed time between initiation and completion of a task - and throughput - the rate at which the system can process tasks - are two fundamental measures of processor performance. Improving throughput or reducing latency results in a better speed-up. The CPUs perform better for latency-oriented tasks, whereas the GPUs are designed for throughput-oriented computing systems. There are some specific measures that are used to decide whether a certain application (or task) is suitable for the GPU or the CPU implementation. The *memory footprint* of a task, the amount of main memory that a program uses or references while running, is the primary measure. For applications that require large memory, the CPUs can be equipped with more random access memory (RAM) to execute the application, whereas the GPUs are very limited in this regard. Other measures are used for evaluating parallel computations and their optimization. The fast memory access of the GPUs and their massively-parallel units are well suited for ordered data patterns. Vector operations perform better on the CPUs, whereas matrix operations are more efficient on the GPUs. It is for such reasons that, as we explained in the main text of the paper, we used a dual combination of CPU + GPU to carry out the

computations.

We emphasize that we use a combination of CPU *and* GPU to carry out the PN/RRN simulation. Using such a combination of two distinct paradigms and programming models for solving a given problem is completely nontrivial. In our work we first generate the PN/RRN using four CPU processors, which are then used in a GPU to solve for the pressure/voltage distribution in the PN/RRN. The percentage of run times spent on the CPU host vary with the size of the network, as well as the number of connected resistors or pores in the network. As the network's size increases, the run time on the CPU also increases due to the limited memory of the GPU. In the problems that we study the GPU code is memory-bounded and most of the time is spent on memory and communication between the nodes. As we show below, in this problem a considerable time is spent for the communications and memory transfer. What this means is that the efficiency will increase dramatically over what is presented in this paper, if the GPU memory also improves.

Our preliminary computations indicated that such a combination of the CPU and GPU yields the most efficient performance because of the following. The distribution of the data in a dual computing system, such as CPU and GPU, is an important factor that can restrict the performance. Although both CPUs and GPUs are capable of performing similar types of calculations, there are several important differences in their execution models and architectures. The number of cores on a CPU is limited, but they are large and fast. GPUs, on the other hand, have hundreds of cores that are slower and, compared with the CPU cores, possess limited capability. It is expensive, in terms of the computer time, to transfer data from one processing unit from the CPU (GPU) to a unit in GPU (CPU), and vice versa. Generating a PN/RRN and solving for the pressure/voltage distribution, are, however, two independent problems that are solved sequentially. The fast memory access of the GPUs and their massively-parallel units are ideal for ordered data patterns. Vector operations are carried out more efficiently on the CPUs, whereas matrix operations are executed faster on GPUs. Thus, it is efficient to use several CPUs to parallelize the PN/RRN generation, because it requires very large computer memory.

The computations were carried out with various PN and RRN sizes in both CPU alone and in GPU, in order to measure the speed-up of the computations. The computing system that we employed consisted of one Intel core i7-4710 CPU (2.5 GHz) with 16 GB of main memory,

and the NVIDIA Geforce GTX 880 graphic card with 1536 cores. All speed-up comparisons have been made with respect to runtime of sequential PN generation and simulation algorithm in C++. Applications were written in CUDA version 6.5 and C++ using Visual Studio 2012.

V. EFFICIENCY OF THE COMPUTATIONS

Since one goal of this paper is demonstrating the efficiency of the computations with standard PN or RRN models, we put the algorithm to use in a most stringent environment. In the former case, the PN network contains long-range correlations between the bonds' permeabilities, as well as anisotropy, as described earlier. In the case of the RRN, we delete a fraction q of the resistors and compute the voltage distribution. As q approaches the percolation threshold of the network, $q = 1/2$, there is usually critical slow-down because the structure of the sample-spanning percolation cluster becomes increasingly tortuous. Thus, a key test of the method is whether the gained efficiency is lost as the percolation threshold is approached.

For a 2D PN/RRN of size $N \times N$ the speed-up of the computations is defined as the ratio of the sequential execution time $t(1, N)$ and the corresponding parallel execution time $t(\mathcal{P}, N)$ with \mathcal{P} processors,

$$S(\mathcal{P}) = \frac{t(1, N)}{t(\mathcal{P}, N)}. \quad (5)$$

In the PN/RRN simulation, the parallel part consists of both the CPUs (for four processors) and the GPUs. Thus, the parallel execution time is the sum of running time for **both** generating the PN/RRN on the CPU and solving the governing equations on the GPU. Another way of measuring the performance of the parallel implementation is the *efficiency* $\mathcal{E}(\mathcal{P})$, defined by

$$\mathcal{E}(\mathcal{P}) = \frac{S(\mathcal{P})}{\mathcal{P}} = \frac{t(1, N)}{\mathcal{P}t(\mathcal{P}, N)}. \quad (6)$$

The efficiency is only used for the parallel implementation of PN/RRN generation.

VI. RESULTS

We carried out extensive computations with a variety of PN and RRN in order to test the speed-up in the computations. In what follows we present and discuss the results.

A. Isotropic networks

Figure 6 presents the effect of the Hurst exponent H on the speed-up of computing the pressure/voltage distribution. The network is isotropic [$\beta_x = \beta_y$ in Eq. (2)], and each data point represents the average of multiple realizations. The speed-up increases with increasing the size of the PN/RRN. For a network with $H = 0.75$ and 3.6 million nodes, the speed-up is 12, more than an order of magnitude improvement in the computations. More importantly, the same speed-up is obtained with a FBM distribution with $H = 0.35$, the case in which the correlations between the permeabilities of conductances are negative, which is typically the case in natural porous media [3]. Thus, the value of the Hurst exponent H has only a minor effect, if at all, on the speed-up of the GPU-based solver, which is strong evidence for the efficiency of the algorithm.

Next, we consider the case of the classical RRN model [58] in which a randomly-selected fraction $p = 1 - q$ of the bonds have a unit conductance, while the rest are insulating. The speed-ups are shown in Fig. 7. As the percolation threshold $q_c = p_c = 1/2$ is approached, the speed-up decreases from about 9.6 for $p = 1$ to about 7.5 very close to p_c . Thus, even though, similar to any critical phenomenon, there is critical slow down in a RRN model as p_c is approach, the speed-up obtained by using the GPU decreases by only about 20 percent, hence indicating the efficiency of the GPU-based computations.

B. Anisotropic networks and permeability anisotropy

As mentioned earlier, natural porous media, as well as many solid materials, are anisotropic. Thus, we studied the effect of the anisotropy parameter β_x/β_y on the performance of CPU+GPU parallel computations. The results are shown in Fig. 8, where we present the speed-up for two values of β_x/β_y and a Hurst exponent of $H = 0.35$. The speed-up is essentially the same that of the isotropic media, and also independent of the value of β_x/β_y . Thus, although in the traditional approaches the computations for anisotropic media take longer times, in the proposed algorithm both the Hurst exponent H and the anisotropy parameter β_x/β_y have a minor effect, if any, on the speed-up gained by the dual CPU-GPU.

Next, we consider the effect of percolation, i.e., attributing zero conductance to the bonds in PNs or RRNs in which the conductances are correlated, with the correlations described by the FBM. The motivation for considering such networks is that natural porous media, in addition to be mostly anisotropic, are highly heterogeneous and contain very low-permeability

zones that contribute very little, if any, to fluid flow. Thus, their permeability or hydraulic conductance may be set to zero. Composite materials that consist of conducting and insulating phases behave the same. But, since the conductance field is correlated, one cannot remove bonds randomly, which would destroy the correlations. Instead, the bonds' conductances are sorted from the smallest to the largest, and a given fraction q of the bonds with the smallest conductances are removed. The results are presented in Fig. 9. In all the case the network contained 3.6×10^6 nodes. The speed-up for all the cases has a trend similar to Fig. 8. Note that as the percolation threshold $q_c = 1/2$ is approached, the speed-up decreases. As pointed out earlier, this represents critical slow down as the percolation threshold is approached. However, even very close to q_c the speed-up is nearly one order of magnitude.

An important problem in modeling of anisotropic porous media is the ratio of the permeabilities K_x/K_y , where x represents the direction that is more or less parallel to the strata that make such porous media anisotropic. There are many empirical estimates of the ratio K_x/K_y in the literature [3] that vary between 1 and 7. Using our efficient solver, and generating the permeability distribution according to Eq. (2), we obtain approximate, but accurate estimates for the permeability anisotropy. The results are presented in Fig. 10. For $H = 0.75$ the anisotropy varies between 0.6 and 1.6, whereas the corresponding numbers for $H = 0.35$, i.e., the much more heterogeneous PNs, are 0.5 and about 2.5.

VII. DISCUSSION

Several important points must be mentioned here. (i) Generally speaking, unlike CPU-based computations, the denser the matrix \mathbf{G} is, the more efficient the GPU-based computations are. Thus, similar calculations for 3D systems and with networks with higher connectivities should yield higher speed-ups. (ii) The calculations with the lattice models of vector transport, such as brittle fracture propagation and similar phenomena will be even more efficient than the scalar transport considered in this paper, because the corresponding matrix \mathbf{G} will be denser, even for 2D systems. (iii) Clearly, any of the past methods of speeding-up the calculations will be more efficient if carried out with the GPUs. (iv) We utilized a single GPU-based solver. Use of several GPUs in parallel should result in very high speed-up factors, a matter that we are currently studying.

VIII. SUMMARY

We proposed an algorithm for simulating the pore-network and random-resistor network models on GPUs. The single GPU-based solver improves the efficiency and running time of the calculations by at least one order of magnitude, when compared with the same calculations with CPU-based simulatorss. The speed-up is even larger for larger networks, and for calculations in which the matrix of the coefficients is denser. Thus, the GPU-based computations make simulation of very large PNs/RRNs possible, regardless of the correlations, anisotropy, or any other pertinent parameter.

ACKNOWLEDGMENTS

This work was supported as part of the Center for Geologic Storage of CO₂, an Energy Frontier Research Center funded by the U.S. Department of Energy, Office of Science, Basic Energy Sciences, under Award number DE-SC0012504.

- [1] S. Torquato, *Random Heterogeneous Materials* (Springer, New York, 2002).
- [2] M.J. Blunt, *Multiphase Flow in Permeable Media* (Cambridge University Press, London, 2017).
- [3] M. Sahimi, *Flow and Transport in Porous Media and Fractured Rock*, 2nd ed. (Wiley-VCH, Weinheim, Germany, 2011).
- [4] B. I. Shklovskii and A.L. Efros, *Electronic Properties of Doped Semiconductors* (Springer, Berlin, 1984).
- [5] M. Sahimi, *Heterogeneous Materials I* (Springer, New York, 2003).
- [6] B. K. Chakrabarti and L. Benguigui, *Statistical Physics of Fracture and Breakdown in Disordered Systems* (Oxford University Press, London, 1997).
- [7] M. Sahimi, *Heterogeneous Materials II* (Springer, New York, 2003).
- [8] *Modelling Critical and Catastrophic Phenomena in Geoscience*, edited by P. Bhattacharyya and B. K. Chakrabarti (Springer, Berlin, 2006).
- [9] D. Stauffer and A. Aharony, *Introduction to Percolation Theory*, 2nd ed. (Taylor and Francis, London, 1994).
- [10] M. Sahimi, *Applications of Percolation Theory* (Taylor and Francis, London, 1994).
- [11] J. Chu, B. Engquist, M. Prodanovic, and R. Tsai, A multiscale method coupling network and continuum models in porous media I: steady-state single phase flow, *Multiscale Model. Simul.* **10**, 515 (2012).
- [12] P.E. Øren, S. Bakke, and O.J. Arntzen, Extending predictive capabilities to network models, *Soc. Pet. Eng. J.* **3**, 324 (1998).
- [13] S. Ovaysi and M. Piri, Direct pore-level modeling of incompressible fluid flow in porous media, *J. Comput. Phys.* **229**, 7456 (2010).
- [14] M. Piri and M.J. Blunt, Three-dimensional mixed-wet random pore-scale network modeling of two- and three-phase flow in porous media. I. Model description, *Phys. Rev. E* **71**, 026301 (2005).

- [15] M. Piri and M.J. Blunt, Three-dimensional mixed-wet random pore-scale network modeling of two- and three-phase flow in porous media. II. Results, *Phys. Rev. E* **71**, 026302 (2005).
- [16] M.J. Blunt, M.D. Jackson, M. Piri, and P.H. Valvatne, Detailed physics, predictive capabilities and macroscopic consequences for pore-network models of multiphase flow, *Adv. Water Resour.* **25**, 1069 (2002).
- [17] M. Prat, Recent advances in pore-scale models for drying of porous media, *Chem. Eng. J.* **86**, 153 (2002).
- [18] O. Borgman, P. Fantinel, W. Luhder, L. Goehring, and R. Holtzman, Impact of spatially correlated pore-scale heterogeneity on drying porous media, *Water Resour. Res.* **53**, 56455658 (2017).
- [19] A.G. Yiotis, D. Salin, and Y. C. Yortsos, Pore network modeling of drying processes in macroporous materials: Effects of gravity, mass boundary layer and pore microstructure, *Transp. Porous Media* **110**, 175 (2015).
- [20] Y. Mehmani, T. Sun, M.T. Balho, P. Eichhubl, and S. Bryant, Multiblock pore-scale modeling and upscaling of reactive transport: Application to carbon sequestration, *Transp. Porous Media* **95**, 305 (2012).
- [21] J.P. Noguees, J.P. Fitts, M.A. Celia, and C.A. Peters, Permeability evolution due to dissolution and precipitation of carbonates using reactive transport modeling in pore networks, *Water Resour. Res.* **49**, 6006 (2013).
- [22] L. Li, C.A. Peters, and M.A. Celia, Upscaling geochemical reaction rates using pore-scale network modeling, *Adv. Water Resour.* **29**, 1351 (2006).
- [23] L.A. Dillard and M.J. Blunt, Development of a pore network simulation model to study nonaqueous phase liquid dissolution, *Water Resour. Res.* **36**, 439 (2000).
- [24] M. Hekmatzadeh, M. Dadvar, and M. Sahimi, Pore-network simulation of unstable miscible displacements in porous media, *Transp. Porous Media* **113**, 511 (2016).

- [25] S. Ghanbarzadeh, M. Prodanovic, and M. A. Hesse, Percolation and grain boundary wetting in anisotropic texturally equilibrated pore networks, *Phys. Rev. Lett.* **113**, 048001 (2014).
- [26] P. Tahmasebi, F. Javadpour, and M. Sahimi, Multiscale and multiresolution modeling of shales and their flow and morphological properties, *Scientific Reports* **5**, 16373 (2015).
- [27] P. Tahmasebi, M. Sahimi, A.H. Kohanpur, and A. Valocchi, Pore-scale simulation of flow of CO₂ and brine in reconstructed and actual 3D rock cores, *J. Pet. Sci. Eng.* **155**, 21 (2017).
- [28] B. Derrida and J. Vannimenus, A transfer-matrix approach to random resistor networks, *J. Phys. A* **15**, L557 (1982).
- [29] J. G. Zabolitzky, D. J. Bergman, and D. Stauffer, Precision calculation of elasticity for percolation, *J. Stat. Phys.* **44**, 211 (1986).
- [30] J.-M. Normand and H.J. Herrmann, Precise numerical determination of the superconducting exponent of percolation in three dimensions, *Int. J. Mod. Phys. C* **1**, 207 (1990).
- [31] A.R. Mehrabi and M. Sahimi, Coarsening of heterogeneous media: application of wavelets, *Phys. Rev. Lett.* **79**, 4385 (1997)
- [32] F. Ebrahimi and M. Sahimi, Multiresolution wavelet coarsening and analysis of transport in heterogeneous media, *Physica A* **316**, 160 (2002).
- [33] M. Sahimi, M. Naderian, and F. Ebrahimi, Efficient simulation of ac conduction in heterogeneous materials at low temperatures, *Phys. Rev. B* **71**, 094208 (2005).
- [34] E. Pazhoohesh, H. Hamzeshpour, and M. Sahimi, Numerical simulation of ac conduction in three-dimensional heterogeneous materials, *Phys. Rev. B* **73**, 174206 (2006).
- [35] A. Aghaei and M. Piri, Direct pore-to-core up-scaling of displacement processes: Dynamic pore network modeling and experimentation, *J. Hydrol.* **522**, 488 (2015).

- [36] J.K. Jasti, G. Jesion, and L. Feldkamp, Microscopic imaging of porous media with x-ray computed tomography, *SPE Form. Eval.* **8**, 189 (1993).
- [37] M. A. Knackstedt, A. P. Sheppard, and M. Sahimi, Pore network modeling of two-phase flow in porous rock: The effect of correlated heterogeneity, *Adv. Water Resour.* **24**, 257 (2001).
- [38] T. T. Tsotsis, H. Patel, B. F. Najafi, D. Racherla, M. A. Knackstedt, and M. Sahimi, An overview of laboratory and modeling studies of carbon dioxide sequestration in coalbeds, *Ind. Eng. Chem. Res.* **43**, 2887 (2004).
- [39] Nvidia Corporation, NVIDIA CUDA programming Guide, <http://docs.nvidia.com/cuda/cuda-c-programming-guide/abstract>
- [40] G. R. Markall, D. A. Ham, and P. H. J. Kelly, Generating optimised finite element solvers for GPU architectures, *AIP Conference Proceedings* **1281**, 787 (2010).
- [41] P. Tahmasebi, M. Sahimi, G. Mariethoz, and A. Hezarkhani, Accelerating geostatistical simulations using graphics processing units (GPU), *Comput. Geosci.* **46**, 51 (2012).
- [42] G.R. Markall, A. Slemmer, D.A. Ham, P. H. J. Kelly, C. D. Cantwell, and S. J. Sherwin, Finite element assembly strategies on multi- and many-core architectures, *Int. J. Numer. Meth. Fluids* **71**, 8097 (2013).
- [43] W. Liu, B. Schmidt, G. Voss, and W. Muller-Wittig, Accelerating molecular dynamics simulations using graphics processing units with CUDA, *Comput. Phys. Commun.* **179**, 634 (2008).
- [44] I. Ufimtsev and T. J. Martinez, Quantum chemistry on graphical processing units. 3. Analytical energy gradients, geometry optimization, and first principles molecular dynamics, *J. Chem. Theor. Comput.* **5**, 2619 (2009).
- [45] R. Olivares-Amaya, M. A. Watson, R. G. Edgar, L. Vogt, Y. Shao, and A. Aspuru-Guzik, Accelerating correlated quantum chemistry calculations using graphical pro-

- cessing units and a mixed precision matrix multiplication library, *J. Chem. Theor. Comput.* **6**, 135 (2010).
- [46] M. Zheng, X. Li, and L. Guo, Algorithms of GPU-enabled reactive force field (ReaxFF) molecular dynamics, *J. Mol. Graphics Model.* **41**, 1 (2013).
- [47] F.J. Molz, H.H. Liu, and J. Szulga, Fractional Brownian motion and fractional Gaussian noise in subsurface hydrology: a review, presentation of fundamental properties, and extensions, *Water Resour. Res.* **33**, 2273 (1997).
- [48] M. Sahimi and S. Mukhopadhyay, Scaling properties of a percolation model with long-range correlations, *Phys. Rev. E* **54**, 3870 (1996).
- [49] M. Sahimi, Long-range correlated percolation and flow and transport in heterogeneous porous media, *J. de Physique I* **4**, 1263 (1994).
- [50] M.A. Knackstedt, A.P. Sheppard, and W.V. Pinczewski, Simulation of mercury porosimetry on correlated grids: evidence for extended correlated heterogeneity at the pore scale in rocks, *Phys. Rev. E* **58**, R6923 (1998).
- [51] H. Dashtian, G.R. Jafari, M. Sahimi, and M. Masihi, Scaling, multifractality, and long-range correlations in well log data of large-scale porous media, *Physica A* **390**, 2096 (2011).
- [52] H. Dashtian, Y. Yang, and M. Sahimi, Nonuniversality of the Archie exponent due to multifractality of resistivity well logs, *Geophys. Res. Lett.* **42**, 10655 (2015).
- [53] B.B. Mandelbrot and J.W. van Ness, Fractional Brownian motion, fractional Gaussian noise, and their applications, *SIAM Rev.* **10**, 422 (1968).
- [54] M. Ansari-Rad, S.M. Vaez Allaei, and M. Sahimi, Nonuniversality of roughness exponent of quasi-static fracture surfaces, *Phys. Rev. E* **85**, 021121 (2012).
- [55] N. Wilt, *The CUDA Handbook: a Comprehensive Guide to GPU Programming* (Addison-Wesley, New York, 2013).
- [56] <http://www.nvidia.com/object/nvidia-kepler.html>

- [57] R. Barrett, M. Berry, T.F. Chan, J. Demmel, J. Donato, J. Dongarra, V. Eijkhout, R. Pozo, C. Romine, and H. van der Vorst, *Templates for the Solution of Linear Systems: Building Blocks for Iterative Methods*, 2nd ed. (SIAM, Philadelphia, 1994).
- [58] S. Kirkpatrick, Percolation and conduction, *Rev. Mod. Phys.* **45**, 574 (1973).

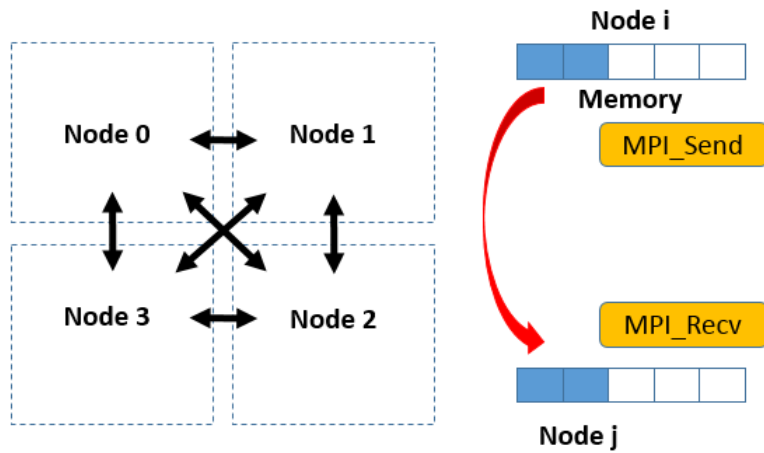


Figure 1: Communications between four nodes (left) and point-to-point communication model.

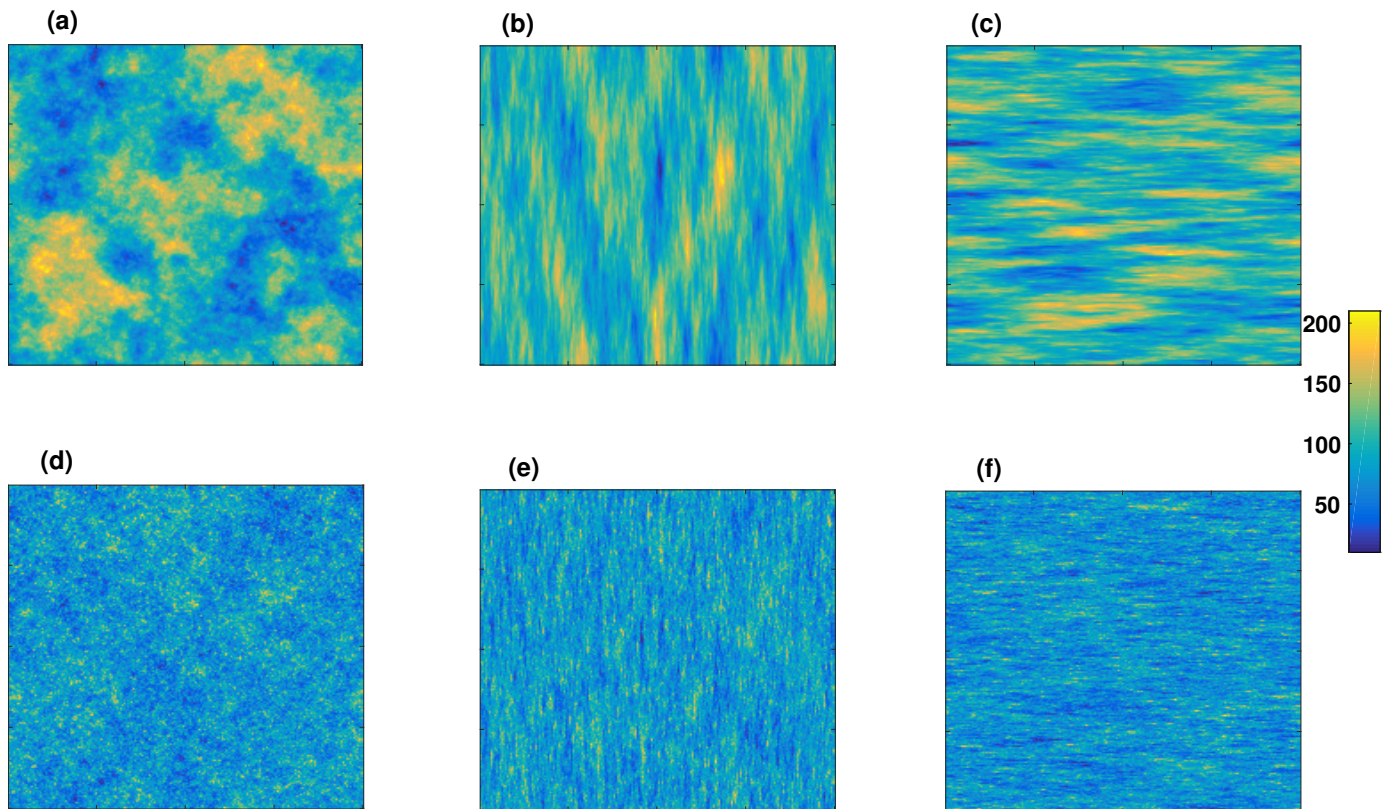


Figure 2: Examples of the networks with correlated conductances. The top and bottom rows show, respectively, the networks with the Hurst exponent of $H = 0.75$ and 0.35 , and β_x/β_y of 1 [(a) and (d)]; $1/5$ [(b) and (e)], and 5 [(c) and (f)].

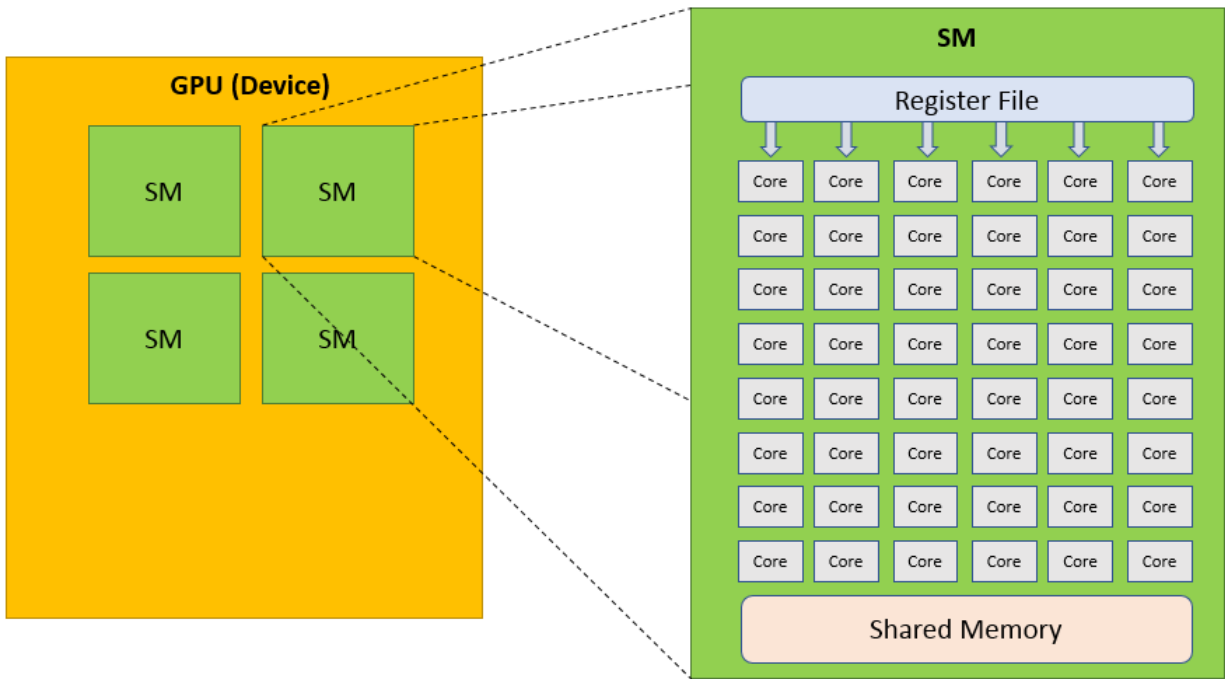


Figure 3: Hierarchy of GPU architecture with four streaming multiprocessors (SM).

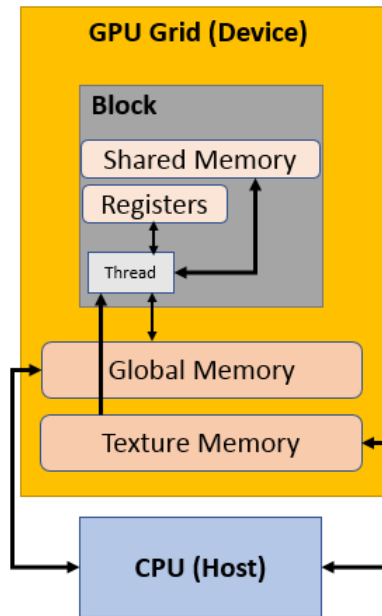


Figure 4: The CUDA memory model.

```


$$r_0 = b - AP_0$$

Mixed
while ( $\|r_k\| > \varepsilon \|r_0\|$ ) {
{
- InnerLoop - Single
Solve :  $Ay = r_k$  within  $\varepsilon^{\text{in}}$ 
}
}

$$P_{k+1} = P_k + \tilde{P}$$

Double

$$r_{k+1} = b - AP_{k+1}$$


$$k = k + 1$$

}

```

Figure 5: Mixed-precision algorithm for the conjugate-gradient method that was used in the computations.

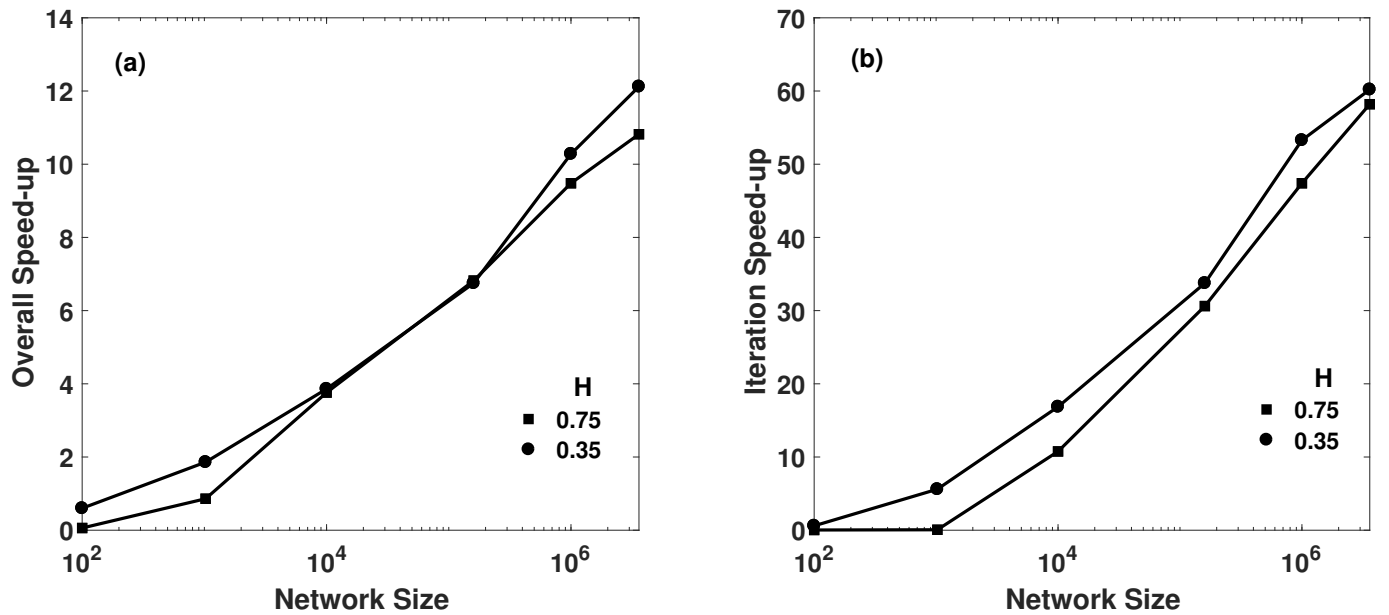


Figure 6: (a) Dependence of the overall speed-up on the size of isotropic networks and the Hurst exponent H . (b) Speed up for one iteration in CG algorithm.

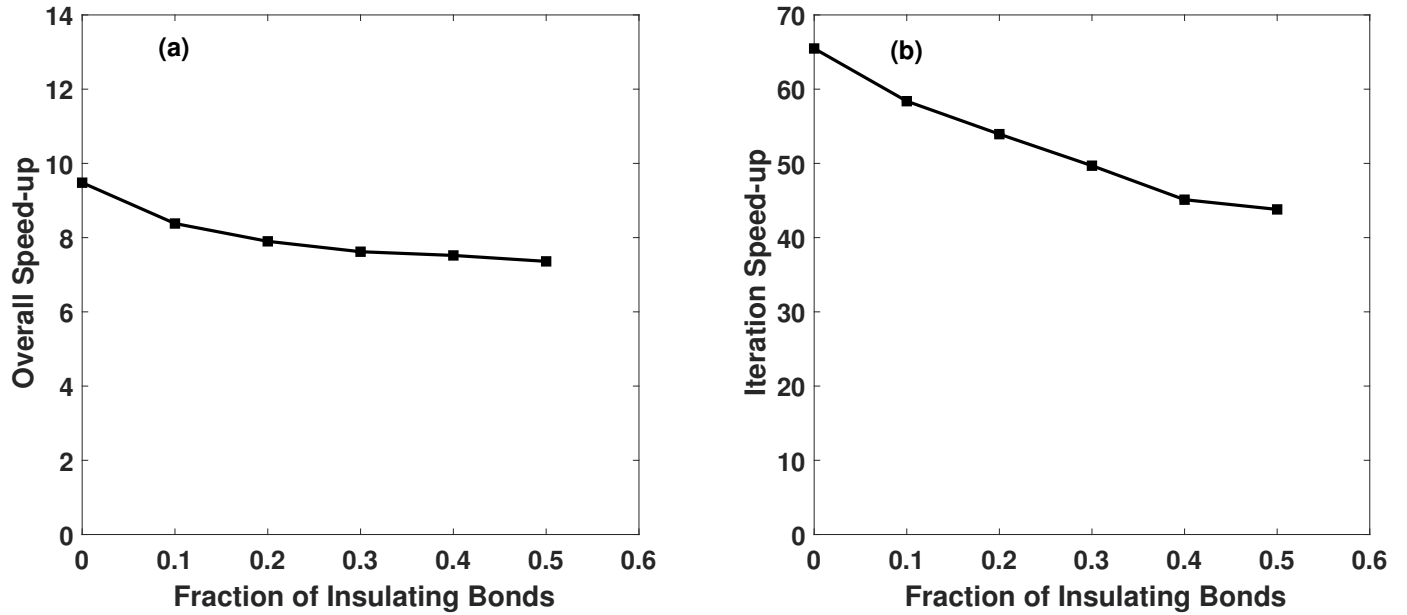


Figure 7: (a) The overall speed-up of the computations with a random resistor network with 3.6×10^6 nodes. (b) Speed up for one iteration in CG algorithm.

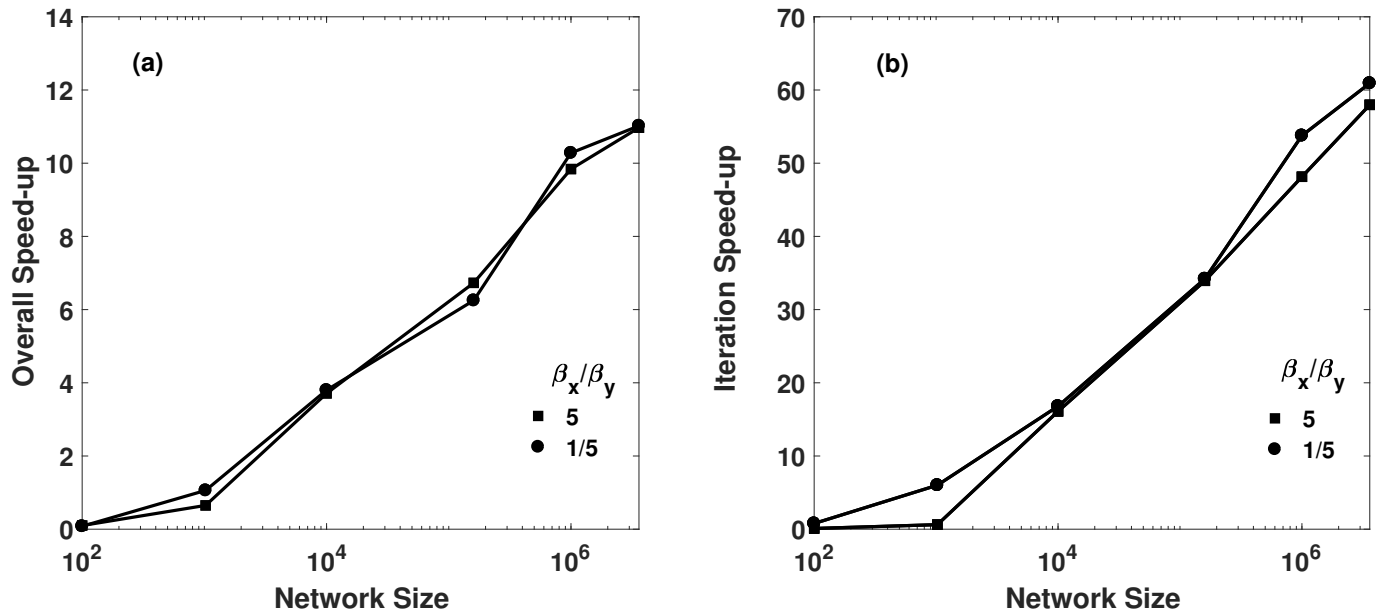


Figure 8: (a) Dependence of the overall speed-up on the size of anisotropic networks and the anisotropy parameter β_x/β_y . The Hurst exponent is $H = 0.35$. (b) Speed up for one iteration in CG algorithm.

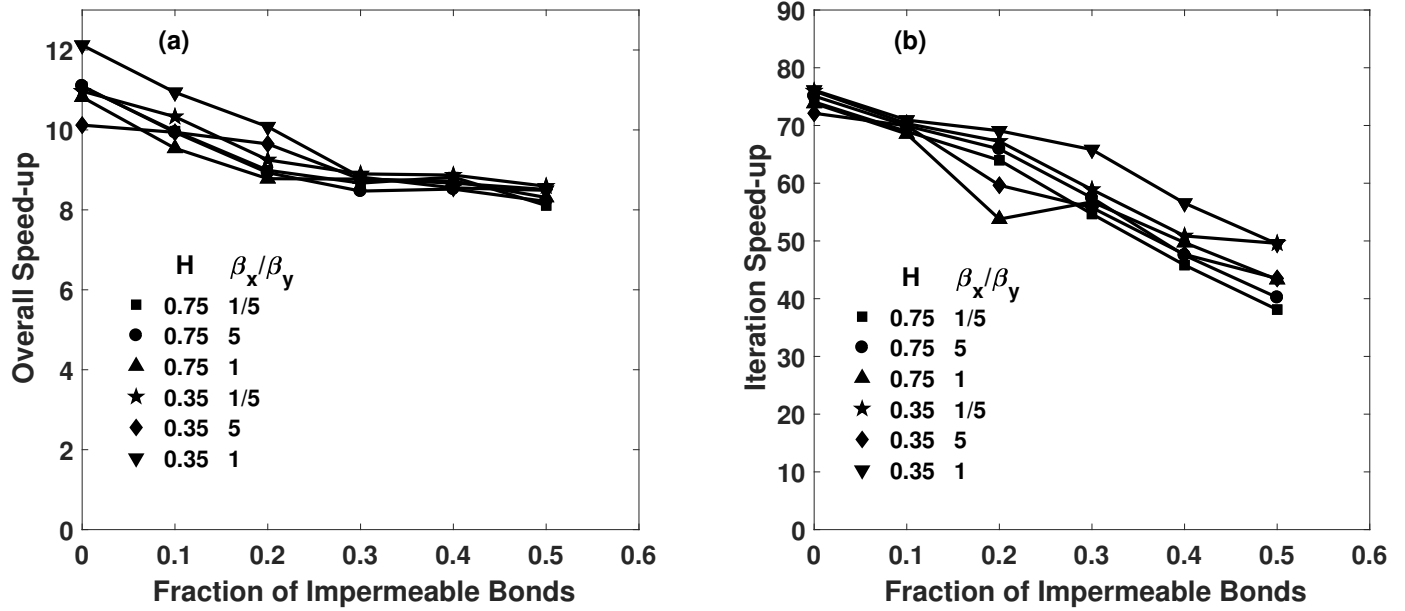


Figure 9: a) Dependence of the overall speed-up of the computations for pore networks with 3.6×10^6 nodes on the fraction of the permeable bonds, the Hurst exponent H and the anisotropy parameter β_x/β_y . (b) Speed up for one iteration in CG algorithm.

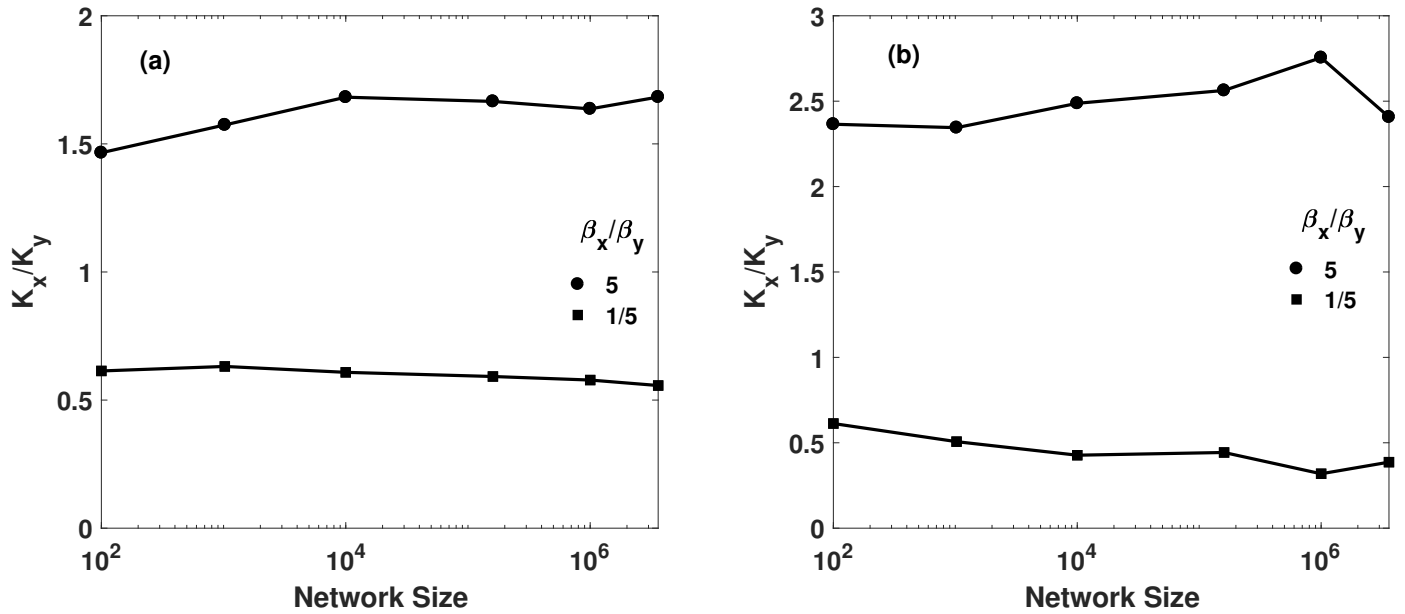


Figure 10: Approximate bounds for the permeability ratio K_x/K_y and their dependence on the anisotropy ratio β_x/β_y and the Hurst exponent H for (a) $H = 0.75$ and (b) $H = 0.35$.